An accreting pulsar with extreme properties drives an ultraluminous x-ray source in NGC 5907

Gian Luca Israel[1,*], Andrea Belfiore[2], Luigi Stella[1], Paolo Esposito[3,2], Piergiorgio Casella[1], Andrea De Luca[2], Martino Marelli[2], Alessandro Papitto[1], Matteo Perri[4,1], Simonetta Puccetti[4,1], Guillermo A. Rodríguez Castillo[1], David Salvetti[2], Andrea Tiengo[5,2], Luca Zampieri[6], Daniele D'Agostino[7], Jochen Greiner[8], Frank Haberl[8], Giovanni Novara[5,2], Ruben Salvaterra[2], Roberto Turolla[9], Mike Watson[10], Joern Wilms[11], Anna Wolter[12]

[1] Osservatorio Astronomico di Roma, INAF, via Frascati 33, I-00078 Monteporzio Catone, Italy

[2] Istituto di Astrofisica Spaziale e Fisica Cosmica, INAF, via E. Bassini 15, I-20133 Milano, Italy

[3] Anton Pannekoek Institute for Astronomy, University of Amsterdam, Postbus 94249, NL-1090GE Amsterdam, The Netherlands

[4] ASI Science Data Center, via del Politecnico snc, I-00133 Roma, Italy

[5] Scuola Universitaria Superiore IUSS Pavia, piazza della Vittoria 15, I-27100 Pavia, Italy

[6] Osservatorio Astronomico di Padova, INAF, vicolo dell'Osservatorio 5, I-35122 Padova, Italy

[7] Istituto di Matematica Applicata e Tecnologie Informatiche "E. Magenes", CNR, via de Marini 6, I-16149 Genova, Italy

[8] Max-Planck-Institut für extraterrestrische Physik, Giessenbachstr., D-85748 Garching, Germany

[9] Dipartimento di Fisica e Astronomia, Università di Padova, via F. Marzolo 8, I-35131 Padova, Italy

[10] Department of Physics and Astronomy, University of Leicester, LE1 7RH Leicester, UK

[11] Dr. Karl-Remeis-Sternwarte and Erlangen Centre for Astroparticle Physics, Sternwartstr. 7, D-96049 Bamberg, Germany

[12] Osservatorio Astronomico di Brera, INAF, via Brera 28, I-20121 Milano, Italy

[*]E-mail: gianluca@oa-roma.inaf.it

Ultraluminous x-ray sources (ULXs) in nearby galaxies shine brighter than any X-ray source in our Galaxy. ULXs are usually modeled as stellar-mass black holes (BHs) accreting at very high rates or intermediate-mass BHs. We present observations showing that NGC 5907 ULX is instead an x-ray accreting neutron star (NS) with a spin period evolving from 1.43 s in 2003 to 1.13 s in 2014. It has an isotropic peak luminosity of $\sim$1000 times the Eddington limit for a NS at 17.1 Mpc. Standard accretion models fail to explain its luminosity, even assuming beamed emission, but a strong multipolar magnetic field can describe its properties. These findings suggest that other extreme ULXs (x-ray luminosity $\geq 10^{41}$ erg s^{-1}) might harbor NSs.

Ultraluminous x-ray sources (ULXs) are observed in off-nucleus regions of nearby galaxies and have x-ray luminosities in excess of a few 10^{39} erg s^{-1}, which is the Eddington luminosity ($L_{\rm Edd}$) for a black hole (BH) of 10 $M_\odot$ (*1*). The $L_{\rm Edd}$ sets an upper limit on the accretion luminosity ($L_{\rm acc}$) of a compact object steadily accreting, since for $L_{\rm acc} > L_{\rm Edd}$ accretion will be halted by radiation forces. For spherical accretion of fully ionized hydrogen, the limit can be written as $L_{\rm Edd} = 4\pi cGMm_{\rm p}/\sigma_{\rm T} \simeq 1.3 \times 10^{38}(M/M_\odot)$ erg s^{-1}, where $\sigma_{\rm T}$ is the Thomson scattering cross section, $m_{\rm p}$ is the proton mass, and $M/M_\odot$ is the compact object mass in solar masses; for a 1.4 $M_\odot$ neutron star (NS), the maximum accreting luminosity is $\sim 2 \times 10^{38}$ erg s^{-1}. The high luminosity of ULXs has thus been explained as accretion at or above the Eddington luminosity onto BHs of stellar origin (<80–100 $M_\odot$), or onto intermediate-mass (10^3–10^5 $M_\odot$) BHs (*2, 3*). However, if the emission of ULXs were beamed over a fraction $b < 1$ of the sky, their true luminosity, and thus also the compact object mass required not to exceed $L_{\rm Edd}$, would be reduced by the same factor. This possibility, together with the recent identification of two accreting NSs associated with the $\sim 10^{40}$ erg s^{-1} M82 X-2 (*4*) and NGC 7793 P13 (*5, 6*) x-ray sources, have brought support to the view that most low-luminosity ULXs likely host a NS (*7*)

or a stellar-mass BH (*8*). For the most extreme ULXs with x-ray luminosity exceeding a few $\times 10^{40}$ erg s^{-1}, BHs with masses in excess of 100 $M_{\odot}$ are still commonly considered (*9, 10*). Despite several searches for coherent x-ray pulsations,no other ultraluminous x-ray source has been found to host a NS so far (*11*).

Within the framework of "Exploring the X-ray Transient and variable Sky", EXTraS (*12*), a project aimed at characterizing the variability of x-ray sources observed with the X-ray Multi-Mirror Mission (*XMM–Newton*) satellite, we have undertaken a systematic search for new x-ray pulsators in the archival data of the European Photon Imaging Camera (EPIC) instrument (*13, 14*). During the analysis of a $\sim$40 ks-long observation carried out from 9 to 10 July 2014 [see table S1 in (*15*)] and pointed to the edge-on spiral galaxy NGC 5907 at a distance of about 17.1 Mpc (*16*), we found a coherent signal in the x-ray emission of NGC 5907 ULX. In fact, a prominent peak at a frequency of $\sim$0.88 Hz (5.8σ detection significance), corresponding to a period $\sim$1.137 s, was detected in the Fourier power spectrum of the 0.2–12 keV light curve of the source. A first period derivative, $\dot{P} \sim -5\times10^{-9}$ s s^{-1}, was also detected. A refined search, including a correction for the $\dot{P}$ term, allowed us to detect the signal in an earlier *XMM–Newton* observation taken on February 2003, and in two observations carried out with the Nuclear Spectroscopic Telescope Array (*NuSTAR*) mission (*17*) taken in July 2014, with periods of $\sim$1.428 s in 2003, and $\sim$1.136 s in 2014 (see Fig. 1 and Table 1). In all cases, a strong first period derivative term is present (see Table 1). The pulse shape is nearly sinusoidal, while the pulsed fraction (the semi-amplitude of the sinusoid divided by the average count rate) is energy dependent and increases from about 12% at low energies ($<$2.5 keV) to $\sim$20% in the hard band ($>$7 keV; Fig. 1).

To derive constraints on the orbital period ($P_{\rm orb}$), we applied a likelihood analysis to the two 2014 *NuSTAR* observations (see supplementary online text), which have the longest baseline.

By assuming a circular orbit (as in the case of M82 X-2), a most-probable $P_{\rm orb} = 5.3^{+2.0}_{-0.9}$ d (see Fig. 2, where 1, 2 and 3σ confidence levels are shown) is inferred, with a projected semi-axis $a \sin i = 2.5^{+4.3}_{-0.8}$ light-s (about 7.5$\times 10^{10}$ cm), where i is the orbital inclination. Though we cannot exclude orbits with period of the order of one month or longer based on the timing analysis alone, we noticed that periods longer then 20 d would require a very high-mass companion ($M > 100\ M_{\odot}$) and are therefore unlikely (see Fig. 2).

In the subsequent analysis, we assume an average spin-up rate of $-(8.1 \pm 0.1) \times 10^{-10}$ s s^{-1} implying a spin-up timescale $P/\dot{P} \sim 40$ yr (*18*). This value is derived from the ratio $\frac{\Delta P}{(T_{14}-T_{03})}$ where ΔP is the difference between the periods measured in February 2003 (T_{03}) and in July 2014 (T_{14}; see Table 1). As this was obtained from a long baseline, it is largely unaffected by the orbital Doppler shift (which is instead present in each single dataset) and, therefore, can be considered a good estimate of the long-term average $\dot{P}$.

The luminosity measured with *Swift*, *Chandra*, *XMM–Newton*, and *NuSTAR* (Fig. S2) display a pronounced variability both on long and short timescales (*19, 20*). The source was detected in $\sim$85% of the observations, its bolometric luminosity (*15*) ranged between $(2.6 \pm 0.3) \times 10^{40}$ and $(2.2 \pm 0.3) \times 10^{41}$ erg s^{-1} (by a factor of about 8). In late 2013, *Chandra* and *XMM–Newton* provided 3σ upper limits on the luminosity of $\sim 3 \times 10^{39}$ and $\sim 4 \times 10^{38}$ erg s^{-1}, respectively (see Fig. S2 and table S1).

If isotropically emitted, the maximum luminosity of NGC 5907 ULX is $\sim$1000 times the Eddington limit for a 1.4-$M_{\odot}$ NS; it thus challenges current models for magnetospheric accretion. NSs can attain highly super-Eddington luminosities only if their magnetic fields is very high: a luminosity of $\sim 1000\ L_{\rm Edd}$ would require a field strength of $>10^{15}$ G (*10, 21*). However, for such a field and the mass inflow rate required to sustain the observed luminosity, the $\sim$1 s rotation of the NS and its magnetosphere would drag matter at the magnetospheric boundary (a distance corresponding to the magnetospheric radius $r_{\rm m}$) so fast that centrifugal

forces exceeds gravity and accretion onto the NS surface is inhibited by the so-called propeller mechanism (*15, 22, 23*).

If the emission of NGC 5907 ULX were beamed over a fraction $b < 1$ of the sky, then the true source luminosity generated by accretion would be lowered by the same factor. A solution is in principle possible for $b \sim 1/100$ and a surface field of $\sim 9 \times 10^{12}$ G, as for such value the maximum luminosity the NS can attain would be compatible with the observations and accretion onto the NS surface could take place, without being inhibited by the propeller. However, the mass accretion rates predicted by this solution would be so low that the corresponding torques would be unable to spin-up the NS at the observed secular rate. Therefore, we conclude that current magnetospheric accretion models which are based on the assumption that the NS magnetic field is purely dipolar are unable to explain the source properties.

A model capable of interpreting the properties of NGC 5907 ULX involves the presence of a multipolar magnetic field at the NS surface of $B_{\rm multi} \sim (0.7\text{–}3) \times 10^{14}$ G, of which only $\sim (0.2\text{–}3) \times 10^{13}$ G is in the dipole component, and a moderate beaming from $b \sim 1/25$ to $1/7$ [see (*15*) and Fig. 3 for details]. With such model, all conditions required for the NS to accrete and generate the factor of $\sim$8 of observed true accretion luminosities and spin-up rate would be met. Such a magnetic field configuration is similar to that envisaged for magnetically-powered neutron star, the so-called magnetars (*24, 25*).

The transient x-ray pulsar we detected in NGC 5907 ULX demonstrates that accreting NSs can achieve extreme luminosities not foreseen in current accretion models. Such high luminosities are often displayed by many ULXs which have previously been classified as accreting black holes. A multi-component strong magnetic field is necessary to account for the properties of NGC 5907 ULX.

References and Notes

1. G. Fabbiano, *Annu. Rev. Astron. Astrophys.* **44**, 323 (2006).

2. J. Poutanen, G. Lipunova, S. Fabrika, A. G. Butkevich, P. Abolmasov, *Mon. Not. R. Astron. Soc.* **377**, 1187 (2007).

3. L. Zampieri, T. P. Roberts, *Mon. Not. R. Astron. Soc.* **400**, 677 (2009).

4. M. Bachetti, *et al.*, *Nature* **514**, 202 (2014).

5. G. L. Israel, *et al.*, *Mon. Not. R. Astron. Soc.* **466**, L48 (2017).

6. F. Fürst, *et al.*, *Astrophys. J.* **831**, L14 (2016).

7. T. Fragos, T. Linden, V. Kalogera, P. Sklias, *Astrophys. J.* **802**, L5 (2015).

8. C. Motch, M. W. Pakull, R. Soria, F. Grisé, G. Pietrzyński, *Nature* **514**, 198 (2014).

9. A. D. Sutton, T. P. Roberts, D. J. Walton, J. C. Gladstone, A. E. Scott, *Mon. Not. R. Astron. Soc.* **423**, 1154 (2012).

10. A. A. Mushtukov, V. F. Suleimanov, S. S. Tsygankov, J. Poutanen, *Mon. Not. R. Astron. Soc.* **454**, 2539 (2015).

11. V. Doroshenko, A. Santangelo, L. Ducci, *Astron. & Astrophys.* **579**, A22 (2015).

12. A. De Luca, *et al.*, *The Universe of Digital Sky Surveys*, N. R. Napolitano, G. Longo, M. Marconi, M. Paolillo, E. Iodice, eds. (2016), vol. 42 of *Astrophys. Space S. Proc.*, p. 291.

13. L. Strüder, *et al.*, *Astron. & Astrophys.* **365**, L18 (2001).

14. M. J. L. Turner, *et al.*, *Astron. & Astrophys* **365**, L27 (2001).

15. Materials and methods are available as supplementary materials on Science Online.

16. R. B. Tully, *et al.*, *Astron. J.* **146**, 86 (2013).

17. F. A. Harrison, *et al.*, *Astrophys. J.* **770**, 103 (2013).

18. V. M. Lipunov, *Sov. Astron.* **26**, 54 (1982).

19. A. D. Sutton, *et al.*, *Mon. Not. R. Astron. Soc.* **434**, 1702 (2013).

20. D. J. Walton, *et al.*, *Astrophys. J.* **799**, 122 (2015).

21. S. Dall'Osso, R. Perna, L. Stella, *Mon. Not. R. Astron. Soc.* **449**, 2144 (2015).

22. A. F. Illarionov, R. A. Sunyaev, *Astron. & Astrophys.* **39**, 185 (1975).

23. L. Stella, N. E. White, R. Rosner, *Astrophys. J* **308**, 669 (1986).

24. C. Thompson, R. C. Duncan, *Mon. Not. R. Astron. Soc.* **275**, 255 (1995).

25. A. Tiengo, *et al.*, *Nature* **500**, 312 (2013).

26. G. L. Israel, L. Stella, *Astrophys. J.* **468**, 369 (1996).

27. C. Gabriel, *et al.*, *Astronomical Data Analysis Software and Systems (ADASS) XIII*, F. Ochsenbein, M. G. Allen, D. Egret, eds. (2004), vol. 314 of *Astronomical Society of the Pacific Conference Series*, p. 759.

28. E. M. Standish, Jr., *Astron. & Astrophys.* **233**, 252 (1990).

29. J. K. Blackburn, *Astronomical Data Analysis Software and Systems IV*, R. A. Shaw, H. E. Payne, J. J. E. Hayes, eds. (1995), vol. 77 of *Astronomical Society of the Pacific Conference Series*, p. 367.

30. G. P. Garmire, M. W. Bautz, P. G. Ford, J. A. Nousek, G. R. Ricker, Jr., *X-Ray and Gamma-Ray Telescopes and Instruments for Astronomy.*, J. E. Truemper, H. D. Tananbaum, eds. (SPIE, Bellingham, 2003), vol. 4851 of *Proceedings of the SPIE.*, pp. 28–44.

31. A. Fruscione, *et al.*, *Society of Photo-Optical Instrumentation Engineers (SPIE) Conference Series* (2006), vol. 6270 of *Proc. SPIE*, p. 62701V.

32. D. N. Burrows, *et al.*, *Space Science Reviews* **120**, 165 (2005).

33. S. M. Ransom, S. S. Eikenberry, J. Middleditch, *Astron. J.* **124**, 1788 (2002).

34. T. Bai, *Astrophys. J.* **397**, 584 (1992).

35. G. Cowan, K. Cranmer, E. Gross, O. Vitells, *European Physical Journal C* **71**, 1554 (2011).

36. K. A. Arnaud, *Astronomical Data Analysis Software and Systems V*, G. H. Jacoby, J. Barnes, eds. (ASP, San Francisco, 1996), vol. 101 of *Astronomical Society of the Pacific Conference Series*, pp. 17–20.

37. E. Anders, N. Grevesse, *Geochimica et Cosmochimica Acta* **53**, 197 (1989).

38. J. Wilms, A. Allen, R. McCray, *Astrophys. J.* **542**, 914 (2000).

39. M. Balucinska-Church, D. McCammon, *Astrophys. J.* **400**, 699 (1992).

40. D. Walton, *et al.*, *Astrophys. J.* **827**, L13 (2016).

41. A. K. H. Kong, *et al.*, *Mon. Not. R. Astron. Soc.* **461**, 4395 (2016).

42. H. Herold, *Phys. Rev. D* **19**, 2868 (1979).

43. S. S. Tsygankov, A. A. Mushtukov, V. F. Suleimanov, J. Poutanen, *Mon. Not. R. Astron. Soc.* **457**, 1101 (2016).

44. K. Parfrey, A. Spitkovsky, A. M. Beloborodov, *Astrophys. J* **822**, 33 (2016).

45. S. Dall'Osso, R. Perna, A. Papitto, E. Bozzo, L. Stella, *Mon. Not. R. Astron. Soc.* **457**, 3076 (2016).

46. N. Rea, *et al.*, *Science* **330**, 944 (2010).

47. K. Y. Ekşi, *et al.*, *Mon. Not. R. Astron. Soc.* **448**, L40 (2015).

48. T. M. Tauris, G. J. Savonije, *Astron. & Astrophys.* **350**, 928 (1999).

49. G. Dubus, J.-P. Lasota, J.-M. Hameury, P. Charles, *Mon. Not. R. Astron. Soc.* **303**, 139 (1999).

50. D. A. Swartz, R. Soria, A. F. Tennant, M. Yukita, *Astrophys. J.* **741**, 49 (2011).

51. J.-F. Liu, J. N. Bregman, J. Irwin, *Astrophys. J.* **642**, 171 (2006).

52. T. M. Tauris, E. P. J. van den Heuvel, G. J. Savonije, *Astrophys. J.* **530**, L93 (2000).

ACKNOWLEDGMENTS

EXTraS is funded from the EU's Seventh Framework Programme under grant agreement no. 607452. This research is based on observations obtained with *XMM–Newton*, an ESA science mission with instruments and contributions directly funded by ESA Member States and NASA. This work also made use of data from *NuSTAR*, a mission led by Caltech, managed by the JPL, and funded by NASA, and from *Swift*, which is a NASA mission with participation of the Italian Space Agency and the UK Space Agency. GLI, PC, LZ and AW acknowledges funding from the ASI–INAF contract NuSTAR I/037/12/0. PE acknowledges funding in the framework of the NWO Vidi award A.2320.0076. AP acknowledges funding from the EU's Horizon 2020 Framework Programme for Research and Innovation under the Marie Skłodowska-Curie grant agreement 660657-TMSP-H2020-MSCA-IF-2014. GLI is grateful to Thomas Tauris for useful comments on an earlier version of the manuscript; PE thanks Alexander Mushtukov for interesting discussions. The EXTraS project acknowledges the usage of computing facilities at INAF's Astronomical Observatory of Catania and Astronomical Observatory of Trieste. The data presented here can be found in the supplementary materials; raw x-ray observations can be retrieved through the ESA/*XMM–Newton* archive interface (http://www.cosmos.esa.int/web/xmm-newton/xsa) and the NASA's ones for *Chandra* (http://cda.harvard.edu /chaser/) and *Swift* (http://heasarc.gsfc.nasa.gov/cgi-bin/W3Browse/swift.pl); see Table S1 for the identification number of the observations.

Table 1 Timing properties of the NGC 5907 ULX pulsar. 1σ confidence level is assumed for the uncertainties. Observational dates are expressed in modified Julian days (MJD).

Start Date	2003 Feb 28	2014 Jul 09	2014 Jul 09	2014 Jul 12
Mission	*XMM–Newton*	*NuSTAR*	*XMM–Newton*	*NuSTAR*
Epoch (MJD)	52690.9	56848.0	56848.2	56851.5
P (s)	1.427579(5)	1.137403(1)	1.137316(3)	1.136042(1)
$\dot{P}$ (10^{-9} s s^{-1})	–9.6(9)	–5.2(1)	–5.0(5)	-4.7(1)

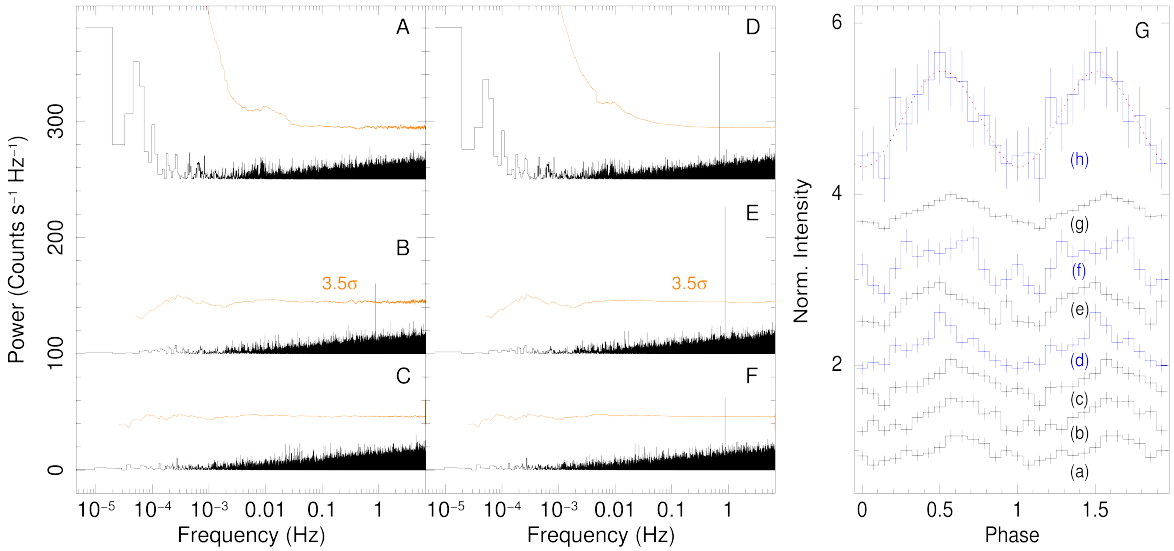

Fig. 1. Detection and study of the pulsations observed in the extreme ULX in NGC 5907. Arbitrarily shifted (along the y-axis) power spectral density (PSD) of the 0.2–12 keV (*XMM–Newton*) and 3–30 keV (*NuSTAR*) NGC 5907 ULX light curves of three out of the four datasets where pulsations have been detected: *XMM–Newton* observations of 2003-20-02 (A) and 2014-07-09/10 (B), and *NuSTAR* observation of 2014-07-09/10 (C). The calculated 3.5σ detection threshold (*26*) is shown for each PSD (light orange solid lines). In the central panel, we show the PSD of the same light curves (A, B and C) after correcting the photon arrival times for the $\dot{P}$ term (D, E and F). The 2014 *XMM–Newton* (black solid lines) and *NuSTAR* (blue solid lines) simultaneous pulse profiles are shown in the right panel (G). From the bottom to the top, energy intervals are: (a) 0.2–2.5 keV, (b) 2.5–4 keV, (c) and (d) 4–7 keV, (e) and (f) 7–12 keV, (g) 0.2–12 keV, and (h) 3–30 keV. Profiles are arbitrarily shifted along the y-axis and two cycles are shown for clarity.

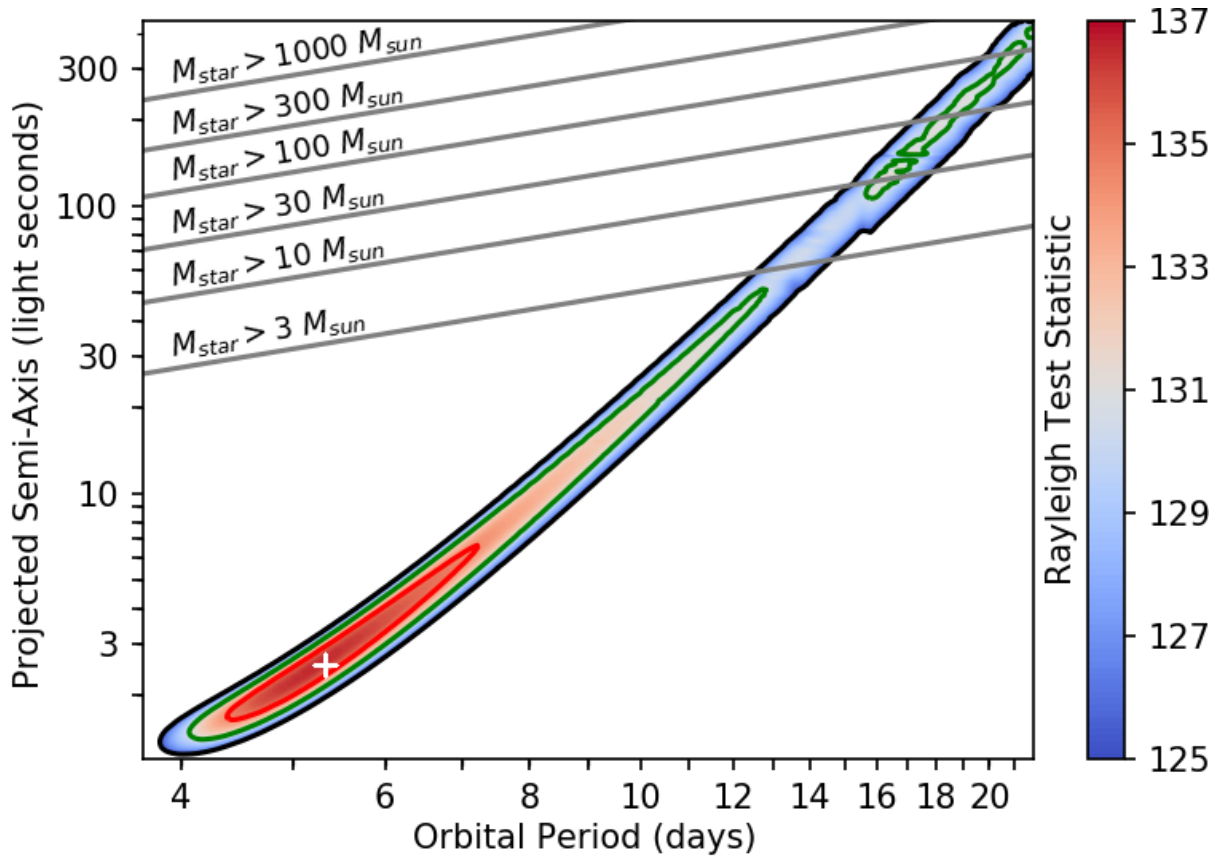

Fig. 2. Orbital period constraints from the likelihood analysis of the 2014 x-ray datasets. Constraints on the orbital parameters of NGC 5907 ULX obtained with a direct likelihood analysis of the 2014 *NuSTAR* observations. For each point in a grid of projected semi-axis a and orbital period $P_{\rm orb}$, we show the maximum Rayleigh test statistic R (*15*). This is obtained scanning over the spin parameters, period P and its time derivative $\dot{P}$, and the epoch of ascending nodes, T_0 as described in (*15*). The best-fit values of a and $P_{\rm orb}$ are indicated with a cross. The contours mark the R confidence levels of 1, 2, and 3σ. The solid parallel lines indicate particular configurations for which the orbital inclination and the masses of the two objects are held fixed. According to Kepler's third law, the mass of the companion to a 1.4 $M_\odot$ neutron star is indicated for a system observed edge-on. As the inclination of the system is unknown, these values must be taken as lower bounds to the actual mass of the companion star.

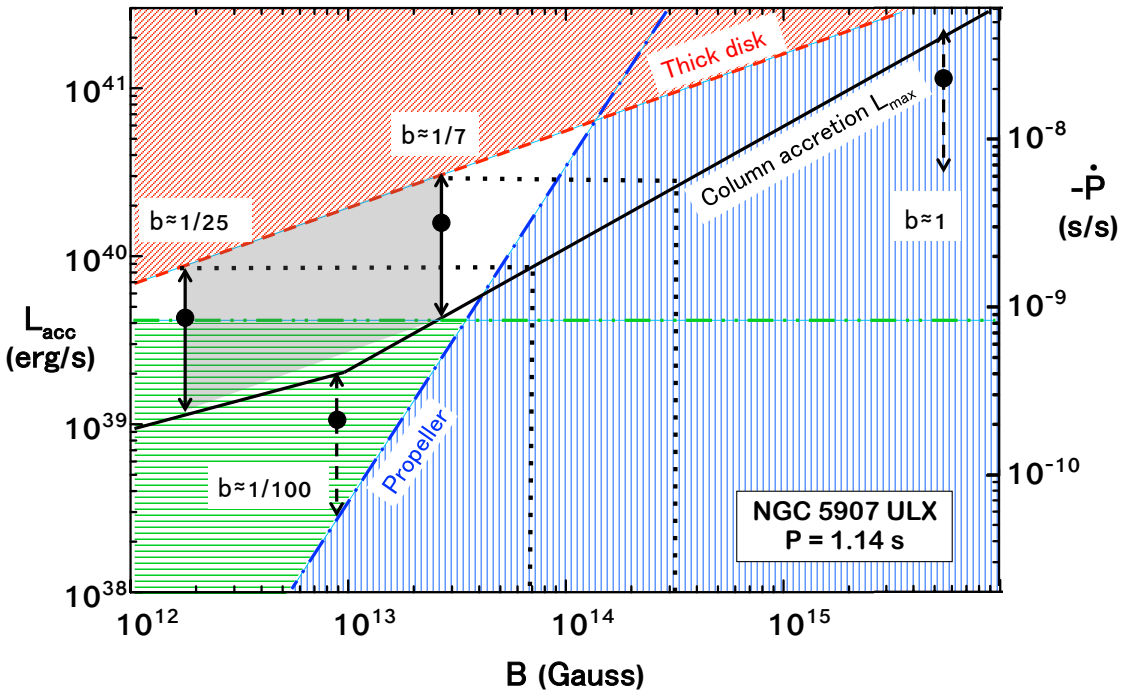

Fig. 3. Accretion luminosity versus surface magnetic field contraints for NGC 5907 ULX. The black solid line represents the maximum luminosity attainable via magnetic column-accretion onto the NS (*10*). Above the dashed (red) line, the energy released in the accretion disk down to the magnetospheric boundary exceeds the Eddington luminosity and the magnetospheric boundary is engulfed with the inflowing matter (*10*). Below the dot-dashed (blue) line, the centrifugal drag by the rotation of the NS magnetosphere exceeds gravity and the propeller regime ensues, where little (if any) accretion takes place (*23*). The double-dotted dashed (green) line represents the secular $\dot{P}$ measured for NGC 5907 ULX (see the relevant Y-axis scale on the right); it is plotted here for the minimum accretion luminosity that is required to give rise to it. Below this line the accretion rate would not be sufficient to spin-up the NS at the observed rate. Double-arrowed segments represent the factor of ∼8 flux variation over which the source was detected. They are shown for different values of the beaming factor (and are correspondingly shifted in accretion luminosity by $b^{-1} = L_{\rm iso}/L_{\rm acc}$): dashed arrows represent solutions which are not viable. A value of $b \sim 1/25$–$1/7$ can reproduce all source features (*15*), for a magnetic dipole surface field of $\sim(0.2\text{–}3) \times 10^{13}$ G and a multipolar surface field of $\sim (0.7\text{–}3) \times 10^{14}$ G.

Supplementary Materials for

An accreting pulsar with extreme properties drives an ultraluminous X-ray source in NGC 5907

Gian Luca Israel,* Andrea Belfiore, Luigi Stella, Paolo Esposito, Piergiorgio Casella, Andrea De Luca, Martino Marelli, Alessandro Papitto, Matteo Perri, Simonetta Puccetti, Guillermo A. Rodríguez Castillo, David Salvetti, Andrea Tiengo, Luca Zampieri, Daniele D'Agostino, Jochen Greiner, Frank Haberl, Giovanni Novara, Ruben Salvaterra, Roberto Turolla, Mike Watson, Joern Wilms, Anna Wolter

* Corresponding author. Email: gianluca@oa-roma.inaf.it

This PDF file includes:

Materials and Methods

Observations and data reduction

We made use of seven *XMM–Newton*, two *Chandra*, five *NuSTAR*, and 151 *Swift* observations; see Table S1 for dates and exposures.

XMM–Newton

In the *XMM–Newton* observations, the positive–negative junction (pn) CCD camera (*13*) of the EPIC instrument was operated in Full Frame mode, with a time resolution of 73.4 ms. The two metal oxide semi-conductor (MOS) CCD detectors (*14*) were set in Full Frame mode, with 2.6 s time resolution. The data reduction was performed with the *XMM–Newton* Science Analysis Software (SAS) v14.0 (*27*). We restricted the analysis to the 'good time' intervals (GTIs) for the relevant CCDs provided in the Processing Pipeline Subsystem (PPS) products available for each observation; this includes the screening out of time periods with flaring particle background. After a careful study of the brightness profile, we chose to extract the source spectra and event lists from 30″-radius circular regions around the *Chandra* source position, $\mathrm{RA} = 15^{\mathrm{h}}15^{\mathrm{m}}58\overset{\mathrm{s}}{.}62$ and $\mathrm{Decl.} = +56^{\circ}18'10\overset{''}{.}3$ (*19*), in the energy ranges of 0.3–10 keV and 0.2–12 keV, respectively (see Fig. S1); the background was estimated locally for each observation. For the timing analysis, the arrival times of the source photons were shifted to the barycentre of the solar system using the SAS tool barycen and assuming the solar system ephemeris DE200 (*28*).

NuSTAR

Each of the two *NuSTAR* telescopes has a focal plane module (FPM), consisting of a solid-state CdZnTe pixel detector surrounded by an anti-coincidence shield (*17*). The two modules, FPMA and FPMB, are sensitive to photons in the 3–78 keV range and event times are recorded with 2-μs accuracy. The raw event files of the observations (Table S1) were processed using the *NuS-*

TAR Data Analysis Software (NuSTARDAS, v1.6.0) which is part of the "General and mission-specific tools to manipulate FITS files" (FTOOLS) package (*29*). Calibrated and cleaned event files were produced using the nupipeline task with standard filtering criteria and the calibration files in the CALDB database (release of 2016-03-15). We used the nuproducts task to extract for each FPM the source and background energy spectra and the barycentre-corrected light-curves in the total range (3–78 keV) and in five energy bands (3–4, 4–5, 5–7, 7–12 and 12–30 keV). We used circular apertures of radius 49″ (corresponding to ∼65% of the encircled energy; see Fig. S1) centred on the *Chandra* source position. Background energy spectra and light-curves were extracted using source-free circular regions with radius 98″ located on the same detector as the source.

Chandra

All *Chandra* observations we used were carried out with the Advanced CCD Imaging Spectrometer (Spectroscopic array, ACIS-S) in full-imaging mode with time resolution of 3.2 s (*30*). To extract the spectra in the 0.2–10 keV energy range, we used the specextract tool of the *Chandra* Interactive Analysis of Observation (CIAO, v4.8) software package (*31*). We used a circular region of 2″ to extract the source counts (see Fig. S1), and the background was estimated locally for each observation. Due to the contiguity of the two observations and the low statistics of the source counts, we combined the two spectra using combine_spectra, which also averages the response matrices.

Swift

The X-Ray Telescope (XRT) on board *Swift* uses a CCD detector sensitive to photons with energies between 0.2 and 10 keV (*32*). All observations used for this work were performed in imaging photon counting (PC) mode, which provides a time resolution of 2.507 s. Data were

processed following standard procedures using FTOOLS (*29*). We extracted the source events from a circular region with radius of 30″ centred on the *Chandra* position of NGC 5907, while to evaluate the background we extracted events from a source-free region of 130″-radius, avoiding the plane of NGC 5907. The ancillary response files were generated with xrtmkarf and accounts for different extraction regions, vignetting and point-spread function corrections. We used the latest available spectral redistribution matrix (v014).

Timing analysis

In the context of the EXTraS project, all the NGC 5907 ULX event lists were screened through a blind search for periodic signals in an automatic fashion following the recipe outlined in (*26*). We found a significant periodic signal from NGC 5907 ULX only in the *XMM–Newton* pn data of the last observation, performed in 2014. Then, we searched again for pulsations all the *XMM–Newton* and *NuSTAR* observations, accounting for a strong time derivative of the spin frequency, and found significant pulsations in 4 cases. We run through a grid in $-2 \times 10^{-8}\,\mathrm{s}^{-1} \leq \dot{\nu}/\nu \leq 2 \times 10^{-8}\,\mathrm{s}^{-1}$, where ν is the spin frequency and $\dot{\nu}$ its first time derivative, by stretching the time series with this transform: $t' = t + \dot{\nu}/\nu \times t^2$, where t is the raw time and t' the transformed one. In this way, a signal with a significant linear trend in frequency is converted into a periodic signal: $\nu \times t' = (\nu + \dot{\nu} \times t) \times t$. We run on each stretched time series a fast Fourier transform, with 2^{16} bins, up to 10 Hz. In only 4 cases out of 7 we detected a peak above the 3σ threshold, trials-corrected; in all four cases the signal was well above the 10σ confidence level. We refined the timing solutions through a direct likelihood approach (see below). We validated our findings by folding the events with PRESTO (*33*) at the detection ephemeris. In 2003 the signal is clearly detected by *XMM–Newton* on February 20 but it is absent only 7 days afterwards, when the source was again observed by *XMM–Newton*, in a very similar observation, at the same count rate as before. In the latter observation, we inferred a 3σ

upper limit on the pulsed fraction of $\sim$12%.

Direct Likelihood Analysis

We refined the ephemeris of single detections and constrained the orbital parameters using a timing technique that relies on unbinned likelihood analysis (*34, 35*). We assume a sinusoidal model for the light curve of the source, where the spin frequency depends on several parameters. When studying individual detections, these parameters are only the spin frequency and its time derivatives. When studying the orbit of the system, besides the spin frequency and its first time derivative, we also have to account for the orbital parameters. In both cases the probability density of detecting a photon at any rotational phase $\theta\left(\overrightarrow{M}, t\right)$, where $\overrightarrow{M}$ is the vector of parameters in the model, can be stated as:

$$P\left(\theta\right) = \frac{1}{2\pi} \times \left(1 + A \times \cos\left(\theta - \phi\right)\right) \tag{S1}$$

where $0 \leq A \leq 1$ is the pulsed fraction and ϕ the spin period phase. In principle, the most likely value of $\left(\overrightarrow{M}, A, \phi\right)$ should be computed by multiplying the likelihood of detecting each photon at the time it was detected, given the set of parameters $\left(\overrightarrow{M}, A, \phi\right)$, and by scanning the parameter space. The maximum log-likelihood with respect to A and ϕ, under the hypothesis that the signal is sinusoidally modulated, approaches the Rayleigh test-statistic for small A. The Rayleigh test-statistic, that we define as

$$R = \frac{2}{N} \times \left[\left(\sum_{i=1}^{N} \sin\theta_i\right)^2 + \left(\sum_{i=1}^{N} \cos\theta_i\right)^2\right] \tag{S2}$$

where $\theta_i = \theta\left(\overrightarrow{M}, t_i\right)$ is the phase expected by our model at the time t_i associated to the i-th photon, out of N, is much faster to compute than the likelihood itself. Therefore, this result allows us to replace the likelihood with R, when searching for the most likely solution and also for studying the likelihood profiles associated to our timing model. In particular, we can con-

sider two nested models, one obtained from the other by freezing k of its m parameters: we can try to reject the nested model by comparing the maxima of their log-likelihood. The increase in log-likelihood produced by further k free parameters follows a χ^2 distribution with k degrees of freedom (dof): $2 \times \Delta \log \mathcal{L}_k \sim \chi^2_k$. By replacing the log-likelihood with R, we can determine a region in a k-dimensional space where the P-value associated to a specific drop in R meets our desired confidence level. In particular, the P and $\dot{P}$ uncertainties are obtained through the likelihood analysis, varying each parameter independently. The epochs were chosen close to the center of each observation in order to minimize the correlation between P and $\dot{P}$.

Constraining the Orbital Parameters

We choose the two *NuSTAR* observations to constrain the orbital parameters of the system, through a direct likelihood analysis, in order to obtain confidence regions and a relation between the orbital period $P_{\rm orb}$ and its projected semi-axis a. We used the two *NuSTAR* observations because they are longer and more closely spaced than the *XMM–Newton* observations, yet a change in $\dot{\nu}$ is apparent, likely resulting from the orbital modulation. We consider a simple model of a circular binary orbit, in order to limit the number of free parameters while still producing some useful constraints. The time delay due to the orbital motion can be written as

$$(\Delta t)_{\rm orb} = a \times \sin\left(\frac{2\pi}{P_{\rm orb}} \times (t - T_0)\right) \tag{S3}$$

where T_0 is the epoch of the ascending node. From this relation, we can correct the event times, accounting for the orbital motion of the system and intrinsic spin frequency derivative $\dot{\nu}$. We can then find the most likely spin frequency ν, pulsed fraction A, and spin phase ϕ, by maximizing the Rayleigh test-statistic R. By scanning over the 5 parameters (2 rotational, and 3 orbital) and fixing a and $P_{\rm orb}$ over a grid, we maximize R over the other 3 parameters at each point in the grid and obtain Fig. 2. Contour levels obtained by using the prescription in the

previous paragraph, mark changes of 2.28, 6.13, 11.73 in R, which correspond to confidence levels of 1, 2, and 3σ, respectively, for a χ^2 distribution with 2 dof in $2 \times \Delta \log \mathcal{L}_k$. Overlaid in the same plot are the lines indicating the maximum allowed mass for a companion to a 1.4-$M_\odot$ NS, compatible with a and $P_{\rm orb}$. While we cannot exclude from likelihood profiles alone an arbitrarily large value of a and $P_{\rm orb}$, we take 30 $M_\odot$ as indicative value for the mass of the companion. Correspondingly, we can estimate an upper limit on the variation of the frequency ν due to the Doppler modulation, at 3σ as:

$$|(\Delta\nu)_{\rm orb}| = \frac{2\pi}{P_{\rm orb}} \times a \times \nu < 7.3 \times 10^{-4}\text{Hz}. \tag{S4}$$

This implies that the difference in ν between 2003 and 2014 is essentially all due to a change in the intrinsic spin period of the pulsar, while the orbital modulation is a secondary effect. Larger masses implies smaller contributions of the orbit to ν. In the same way we can derive from the above relation for $(\Delta t)_{\rm orb}$, an estimate of the amplitude of the time derivative of the spin frequency $\dot{\nu}$ as

$$|(\Delta\dot{\nu})_{\rm orb}| = \left(\frac{2\pi}{P_{\rm orb}}\right)^2 \times a \times \nu < 3.1 \times 10^{-9}\text{Hz}s^{-1}. \tag{S5}$$

This implies that the discrepancy between the secular spin-up and the instantaneous spin-up measured in the single observations cannot fully be accounted for by the orbital modulation alone.

Phase Averaged and Pulse Phase Spectroscopy

We fit simultaneously the *XMM–Newton*, *Chandra* and *NuSTAR* spectra using XSPEC v.12.9.0 (*36*). For all tested models, we added a multiplicative factor to account for the different normalizations and uncertainties in the inter-calibration of the various instruments. We grouped *XMM–Newton* spectra so as to have at least 100 counts per energy bin and *Chandra* and *NuSTAR* ones with a minimum of 50 counts per bin. We analyzed only data in the 0.3–10 keV band

for *XMM–Newton* and *Chandra* spectra and in the 3–30 keV band for *NuSTAR* spectra. All luminosities (Table S1) are in the 0.3–10 keV energy band and upper limits are at 3σ confidence level. In the two *NuSTAR* and *XMM–Newton* observations performed on 2013-11-06, we did not detect NGC 5907 ULX down to a 3σ limiting luminosity of 2×10^{39} erg s^{-1} and 3×10^{38} erg s^{-1}, respectively, in agreement with the results by (*20*).

Spectra are fit equally well by a broken power law (bknpow in XSPEC) or a Comptonized photons in a hot plasma model (comptt) or a multi-temperature disk blackbody with a power-law dependence of temperature on radius (diskpbb), all modified for the interstellar absorption, while simple thermal models or a power law does not fit adequately the data (reduced $\chi^2 > 2$). In our analysis we assumed chemical abundances from both (*37*) and (*38*) and cross sections from (*39*), providing consistent values for the single component parameters, with the latter abundances providing a higher, about 30%, interstellar absorption value. For all models, the spectrum of NGC 5907 ULX appears to change between the observations.

For the bknpow model, the best spectral fit, obtained by keeping the lower-energy photon index free, resulted in a reduced χ^2 of 1.07 (898 dof). The best-fit parameters are $N_{\rm H} = (5.36 \pm 0.01) \times 10^{21}$ cm^{-2} for the absorption column, $E_{\rm break} = (6.7 \pm 0.2)$ keV for the energy of the break, $\Gamma_2 = 2.9 \pm 0.1$ for the power-law photon index above $E_{\rm break}$ and $\Gamma_1^{2003} = 1.58 \pm 0.02$, $\Gamma_1^{2012} = 1.28 \pm 0.03$, $\Gamma_1^{2013} = 1.91 \pm 0.03$, $\Gamma_1^{2014} = 1.53 \pm 0.02$ for the power-law photon index below $E_{\rm break}$ for the four epochs (see also Table S1).

For the comptt model, the resulting best fit, obtained by keeping free the plasma temperature, has a reduced χ^2 of 1.09 (898 dof). The best-fit parameters are $N_{\rm H} = (5.45 \pm 0.01) \times 10^{21}$ cm^{-2}, Wien temperature of the input soft photons $kT_0 = (6.8 \pm 2.3) \times 10^{-2}$ keV, optical depth $\tau = 7.69 \pm 0.01$, and plasma temperature $kT^{2003} = (2.5 \pm 0.1)$ keV, $kT^{2012} = (3.8 \pm 0.2)$ keV, $kT^{2013} = (2.0 \pm 0.2)$ keV, $kT^{2014} = (2.6 \pm 0.1)$ keV for the four epochs.

Finally, for the diskpbb model, the resulting best fit, assuming the disk temperature free to

vary, has a reduced χ^2 of 1.06 (898 dof). The best-fit parameters are $N_{\rm H} = (4.86 \pm 0.01) \times 10^{21}$ cm^{-2}, temperature at the inner disk radius $T_{in} = (3.4 \pm 0.1) \times 10^{-2}$ keV and exponent of the radial dependence of the disk temperature $p^{2003} = (5.92 \pm 0.01) \times 10^{-1}$, $p^{2012} = (6.62 \pm 0.01) \times 10^{-1}$, $p^{2013} = (6.58 \pm 0.02) \times 10^{-1}$, $p^{2014} = (6.03 \pm 0.01) \times 10^{-1}$ for the four epochs.

The inferred 0.3-10 keV luminosity measures are not strongly dependent on the models: in all cases the differences between the assumed models are within 1%. The luminosities reported in Fig. S2 and Table S1 were instead the bolometric one inferred by adopting the bknpow model.

We do not know why pulsations are detected only in two out of five *XMM–Newton* data sets with sufficient time resolution, but we note that the spectral properties of the data (2003 and 2014) in which pulsations were detected are similar to each other and different from the others. This is shown in Fig. S3, where we compare the spectra (fit with a bknpow model) collected in 2003, 2013 and 2014 (the *XMM–Newton* and *NuSTAR* data obtained in 2013 are representative of the source spectral properties during which pulsations are not detected). For the two EPIC-pn data sets collected in 2003 and 2014, where pulsations are detected, we also carried out a pulse phase spectroscopy to study the possible presence of spectral variations as a function of the pulse phase. The results of the analysis confirms the presence of a phase shift of 0.15$\pm$0.03 cycles between soft ($<$5 keV) and high ($>$7 keV) energies in the 2014 EPIC-pn data (see Fig. S4.), while there is marginal significant dependence of the spectral parameters as a function of phase.

Swift monitoring

For each observation, we estimated the source flux by fitting the 0.3–10 keV spectrum with a broken power-law model (modified for the interstellar absorption), with the following (fixed) parameters: absorption $N_{\rm H} = 5.3 \times 10^{21}$ cm^{-2}, break energy $E_{\rm break} = 6.7$ keV, photon indices $\Gamma_1 = 1.6$ for $E < E_{\rm break}$ and $\Gamma_2 = 2.9$ for $E > E_{\rm break}$. Fig. S2. shows the long-term

x-ray light curve of NGC 5907 ULX (see also Table S1). The luminosity was computed over the 0.3–10 keV energy range from the unabsorbed flux assuming a distance of 17.1 Mpc; in those cases in which the count rate in an observation was compatible with zero, we set an upper limit at the 3σ level. A $\sim$50% modulation on a time scale of $\approx$80 d (*40*) is apparent in the light curve obtained from 151 *Swift* observations from 2010 to 2016 (Fig. S2 and Table S1). The power spectrum peak at 81 ± 2 d has a ratio of centroid frequency to full width at half-maximum (a standard indicator for the coherence of a signal) of $\leq$50, amid typical values for quasi periodic oscillations and periodic signals, indicating that the modulation might not be strictly coherent. A super-orbital modulation of $\sim$55 day has been reported for M82 ULX-2 and interpreted as caused by a radiation-driven warping of the accretion disc (*41*). Considering that the M82 ULX-2 has an orbital period of 2.5 day and assuming a linear scaling, the orbital period of NGC 5907 ULX would be approximately 4 day, which is similar to our estimate based on the *NuSTAR* 2014 data (under the hypothesis that the two systems have a similar evolutionary history).

Supplementary text

The accretion models

Accreting NSs release a luminosity of $L_{\rm acc}(R) = GM\dot{M}/R$ (where M is the NS mass, $\dot{M}$ the mass accretion rate and G the gravitational constant). $L_{\rm acc}$ may exceed $L_{\rm Edd}$ by a large factor if the NS surface magnetic field is very high ($B > 10^{13}$ G), so that electron scattering cross sections in the extraordinary mode are reduced for photon energies below the cyclotron energy $E_c \sim 12\, B_{12}$ keV (where $B_{12} = B/10^{12}$ G) and a high radiation flux can escape without halting the accretion flow (*42*). Detailed calculation show that magnetically-funneled column accretion onto the NS poles can give rise to a luminosity of $\times 10^3\, L_{\rm Edd}$ if B is $\sim 5 \times 10^{15}$ G (*10*). The solid line in Fig. 3 shows the maximum luminosity that can be attained by magnetically-

funneled column accretion onto the NS poles as a function of the NS surface magnetic field [adopted from Fig.5 of (*10*)]; above $\sim 10^{13}$ G it is well approximated by $L_{39} \sim 0.35\, B_{12}^{3/4}$, where $L_{39} = L_{\rm acc}/10^{39}$ erg s^{-1}.

Accretion at very-high rates is required to attain highly super-Eddington luminosities; a number of conditions must be met for it to take place. First, the flow towards the magnetospheric boundary, where the B-field begins to control the accreting plasma, must be mediated by a disk, so that radiation emitted at the NS can escape unimpeded in a range of directions. For the magnetospheric radius $r_{\rm m}$ we adopt the standard expression

$$r_{\rm m} = \frac{\xi \mu^{4/7}}{\dot{M}^{2/7}(2GM)^{1/7}} = 3.3 \times 10^7\, \xi_{0.5}\, B_{12}^{4/7}\, L_{39}^{-2/7}\, R_6^{10/7}\, m_{1.4}^{1/7}\ {\rm cm} \qquad \text{(S6)}$$

where $\mu = BR^3/2$ is the NS dipole magnetic moment, B is the magnetic field strength at the poles of the NS, R is the NS radius, and ξ is a factor < 1 expressing the magnetospheric radius as a fraction of the Alfvén radius. The value on the right hand side was evaluated by using $\xi_{0.5} = \xi/0.5$, $R_6 = R/10^6$ cm and $m_{1.4} = M/1.4\, M_\odot$.

The accretion disk must remain geometrically thin (with height/radius $<$1) down to the magnetospheric radius ($r_{\rm m}$, where matter is channeled along the NS B-field lines), so as not to engulf the magnetospheric boundary at high latitudes. This requires that the accretion energy released in the disk is sub-Eddington, *i.e.* $L_{\rm disk}(r_{\rm m}) = GM\dot{M}/2r_{\rm m} < L_{\rm Edd}$. The corresponding threshold

$$L_{\rm acc}^{\rm max} = 6.8 \times 10^{39}\, \xi_{0.5}^{7/9}\, B_{12}^{4/9}\, R_6^{1/3}\, m_{1.4}^{8/9}\ {\rm erg\,s^{-1}} \qquad \text{(S7)}$$

is plotted as a dashed line in Fig. 3.

Another condition is that the angular velocity of the disk at $r_{\rm m}$ must be higher than the NS angular velocity, so that the centrifugal drag exerted by the magnetic field lines as matter enters the magnetosphere is weaker than gravity and matter can accrete onto the NS surface. This condition translates into $r_{\rm m} < r_{\rm cor}$, where $r_{\rm cor} = \left(\frac{GMP^2}{4\pi^2}\right)^{1/3}$ is the corotation radius. In

the opposite case, $r_{\rm m} > r_{\rm cor}$, the centrifugal drag by the magnetosphere at $r_{\rm m}$ exceeds gravity, accretion is almost completely halted by the so-called propeller mechanism and the NS enters a regime in which the emitted luminosity is much lower (*22, 23, 43–45*). The minimum accretion luminosity below which the NS enters the propeller regime is obtained by setting $r_{\rm m} = r_{\rm cor}$,

$$L_{\rm acc}^{\rm min} = 2.8 \times 10^{36}\, \xi_{0.5}^{7/2}\, B_{12}^{2}\, R_{6}^{5}\, m_{1.4}^{-2/3}\, {\rm erg\,s^{-1}} \tag{S8}$$

This is plotted as a dot-dashed line in Fig. 3, for spin period of $P = 1.14$ s

If NGC 5907 ULX emitted isotropically a maximum luminosity $L_{\rm max,iso} \sim 2 \times 10^{41}$ erg s^{-1}, then a NS B-field at the base of the accretion column of $\sim 5 \times 10^{15}$ G would be required (*10*). However, for such B and a spin period of $P \sim 1$ s, the NS would be deep in the propeller regime and accretion would not take place (see Fig. 3). On the contrary, the NS in NGC 5907 ULX was observed accreting over the luminosity range from $L_{\rm max,iso} \sim 2 \times 10^{41}$ erg s^{-1} to $L_{\rm min,iso} \sim L_{\rm max,iso}/8$ (shown by the double-arrowed dashed segment on the right of Fig. 3), at a time-averaged luminosity of $L_{\rm avg,iso} \sim 10^{41}$ erg s^{-1} (shown by the black circle on the double-arrowed segment in Fig.3).

This inconsistency can be avoided if the source emission is beamed by a factor $b < 1$, so that its isotropic equivalent luminosity is $L_{\rm iso} = L_{\rm acc}/b$ and the accretion luminosity $L_{\rm acc}$ is reduced accordingly. We require that at the accretion luminosity corresponding to the minimum (detected) isotropic luminosity, *i.e.* $L_{\rm min,acc} = L_{\rm min,iso} b$ the propeller mechanism has not yet set in, and that the surface B-field is such that the maximum accretion luminosity corresponding the maximum isotropic luminosity ($L_{\rm max,acc} = L_{\rm max,iso} b$) can be generated in the accreting column. A beaming factor of $b \sim 1/100$ and a field of $B \sim 9 \times 10^{12}$ G satisfies both requirements, as shown in Fig. 3 by the double-arrowed dashed segment on the left (note that in this case the requirement that the accretion disk remains geometrically thin at $r_{\rm m}$ does not provide any additional constraint). One has to further verify that the mass accretion rate implied by $b \sim$

$1/100$ would be sufficient to cause the observed secular spin-up rate. Accretion torques are highest when all the angular momentum of matter at $r_{\rm m} = r_{\rm cor}$ is transferred to the neutron star; this condition translates into an upper limit on the NS period derivative of $\dot{P} < \dot{M}\, r_{\rm cor}^2 P/I$ (where $I \sim 10^{45}$ g cm^2 is the NS moment of inertia). For the (time-averaged) accretion rate of $\dot{M} \sim 5 \times 10^{18}$ g s^{-1} corresponding to $L_{\rm avg,iso}$ for $b \sim 1/100$, the above limit gives $\dot{P}$ <- 2 $\times 10^{-10}$ s s^{-1} which is a factor of $\sim$4 smaller than the secular value derived from the data. The latter is plotted as a double-dotted dashed line in Fig.3, with the conversion factor between L_{acc} and $\dot{P}$ shown by the Y-axis scale on the right side. Note also that the measured $\dot{P}$ might be affected by spin-down torques that set in during the intervals in which the NS accreted at low levels or was in off-states, possibly in the propeller regime. Therefore we conclude that this solution is untenable.

Implicit in standard accretion theory onto magnetic stars is the assumption that the B-field is purely dipolar. By analogy with magnetars (*24, 25*), we then consider the possibility that the B-field at the base of the accretion column is dominated by higher multipoles rather than being a simple dipole [we note that this assumption does not necessarily imply the presence of a magnetar, the properties of which depend instead on the inner B-field (*46*); see also (*47*)] and that only the dipole component survives at the magnetospheric radius ($r_{\rm m} \sim 10^8$ cm $\sim 100R$), by virtue of its weaker radial dependence. Such configuration retains a high value of the B-field at the NS surface, thus permitting the release of super-Eddington luminosities, while easing the propeller constraint at $r_{\rm m}$. In practice one has to impose two conditions for the dipole field at $r_{\rm m}$, namely that the accretion disk remains thin for $L_{\rm max,acc} = L_{\rm max,iso} b$ and that the propeller has not yet set in for $L_{\rm min,acc} = L_{\rm min,iso} b$. A dipole field at the surface $B \sim 3 \times 10^{13}$ G and a beaming of $b \sim 1/7$ satisfy both conditions (see the right double-arrowed solid segment in Fig. 3).

For the time-averaged accretion rate implied in the case $b \sim 1/7$ ($\dot{M} \sim 7 \times 10^{19}$ g s^{-1}),

we derive a maximum spin-up $\dot{P}$ of about -3×10^{-9} s s^{-1}, which accounts for the measured secular value (this can also be seen in Fig. 3: the black circle representing the time-averaged accretion luminosity for the $b = 1/7$ double-arrow lies above the double-dotted dashed line). Somewhat smaller values of the beaming factor are also allowed, for instance $b \sim 1/25$. For such a value, the observed $\dot{P}$ could still be produced (see the left double-arrowed solid segment in Fig. 3, whose black circle coincides with the double-dotted dashed line); moreover the minimum accretion luminosity could attain a factor of $\sim$4 value without yet triggering the propeller mechanism. The range of allowed solutions is represented by the grey-shaded parallelogram in Fig. 3 and comprises surface dipole fields between $\sim$0.2 and $\sim 3 \times 10^{13}$ G. Corresponding to that range, a multipolar field $B_{\rm multi} > (0.7\text{–}3) \times 10^{14}$ G at the NS surface (the reason why these should be regarded as lower limits is explained below) is required to attain the maximum accretion luminosity of $L_{\rm max,acc} = (0.8\text{–}3) \times 10^{40}$ erg s^{-1} implied by solutions with $b \sim 1/25$–$1/7$. We thus conclude the properties of NGC 5907 ULX provide robust evidence in favor of a multipolar B-field component at the star surface that is about an order of magnitude larger than the dipole field component.

Finally, we remark that the model of (*10*), which the above discussion of the maximum luminosity of magnetic-column accretion builds on, assumes a dipole magnetic field. Extending the treatment to the case of higher order multipoles requires detailed modeling. Yet some estimates can be made for a accretion columns dominated by multipolar fields. An approximate value of the accretion luminosity using eq. (8) of ref. (*10*), is obtained by retaining the dependence of the scattering cross section on B ($\sigma_\perp \sim B^{-2}$), which in turn changes with height inside the column, h (their expression (13) for the dipole; for higher order multipoles the field decays faster with h). The maximum luminosity $L_{\rm max}$ roughly corresponds to $H/R \sim 1$, where R is the star radius and H is the total height of the emitting column. We estimate that the maximum luminosity is a factor of a few lower for higher multipole fields than for dipoles. This is in line

with expectations, since the steeper decrease of multipolar fields with height implies a larger cross section and hence a smaller attainable luminosity. This is the reason why the value we inferred above for $B_{\rm multi}$ should be regarded as lower limits.

The nature of the system

Before facing the possible nature of the binary system we briefly comment on the hypothesis that the source is not part of NGC 5907. The possibility that NGC 5907 ULX is a foreground high mass or low mass x-ray binary in our Galaxy is unlikely due to the high Galactic latitude and the Hubble Space Telescope (*HST*) optical limit of 25 mag (*19*).

The observed spin-up rate of NGC 5907 ULX and the accretion scenario imply an accretion rate at least of $\dot{M} \sim 10^{19}$ g s^{-1}. A value this high rules out accretion through a wind. Assuming Roche lobe overflow onto a NS and an orbital period of ~ 4 days, stellar companions capable to fill the Roche lobe are: (i) a star with $M_2 > 10$–15 $M_\odot$ at terminal age main sequence or in the giant phase; (ii) a supergiant with a mass in excess of 10 $M_\odot$; (iii) a giant with $M_2 \sim 1\ M_\odot$; (iv) a giant with $M_2 = 2$–6 $M_\odot$. We note that if the orbital period is longer than 4 days, a terminal age main sequence star would underfill its Roche lobe. These high-mass binary system (HMXB, i and ii), low-mass binary system (LMXB, iii), and intermediate-mass binary system (IMXB, iv) scenarios are consistent with the upper limits derived from *HST* images (*19*). In the first two cases, owing to the large mass ratio ($q = M_2/M_1 \gg 1$, with $M_1 = 1.4\ M_\odot$), the mass transfer would be unstable, unless the system loses mass at a very high rate through powerful outflows and/or winds (*7*). As an upper limit for the evolutionary timescale, we can assume that the evolution proceeds on an approximately thermal timescale $t_{\rm th}$. A rough estimate of the mass transfer rate can be obtained from $\dot{M}_2 \approx M_2/t_{\rm th}$. We then have $t_{\rm th} \approx 7 \times 10^4$ yr and $\dot{M}_2 \approx 10^{22}$ g s^{-1} for the scenario (i), and $t_{\rm th} \approx 3 \times 10^4$ yr and $\dot{M}_2 \approx 2 \times 10^{22}$ g s^{-1} for (ii). The estimated upper limit on $\dot{M}_2$ is largely in excess of that required to power NGC 5907 ULX .

Thus, provided that the system can be stabilized through strong mass losses, these numbers are consistent with the possibility that NGC 5907 ULX is an HMXB accreting above the Eddington limit. On the other hand, if the outflows are not efficient, the system will enter the common envelope phase and be very short lived.

In the LMXB scenario, the lower mass ratio allows stable mass transfer. During the core He burning phase, the evolution likely proceeds on a nuclear timescale $t_{\rm nuc}$ while, during the H and He shell burning phases, it proceeds on a thermal timescale. Assuming that $\dot{M}_2 \approx M_2/t_{\rm nuc,th}$, we have $t_{\rm nuc} \approx 7 \times 10^7$ yr and $\dot{M}_{2,\rm nuc} \approx 10^{19}$ g s^{-1} for the He core burning phase. The orbital separation increases and exceeds rapidly a few tens of days (*48*), which is difficult to reconcile with the interval estimated from our likelihood analysis. The inferred mass transfer rate is sufficiently high to guarantee a stable accretion disc (*49*), but follows a bit short of what is needed to power NGC 5907 ULX even accounting for beaming. In addition, we note that LMXB ULXs seem to be preferentially associated with elliptical galaxies and their average luminosity is lower than that of ULXs in spiral galaxies (*50*). The fraction of ULXs associated with old stellar populations in spiral galaxies is rather low (*51*), implying that ULX LMXB systems possibly similar to NGC 5907 ULX might not be common.

The last possibility is that of an intermediate mass donor. Post-main sequence stars of $\sim$2–6 $M_\odot$ without deep convective envelopes are able to survive a highly super-Eddington mass transfer phase and remain dynamically stable for a few hundred thousands years, while maintaining orbital periods of a few days (*52*). This IMBH channel appears to be consistent with the inferred properties of NGC 5907 ULX.

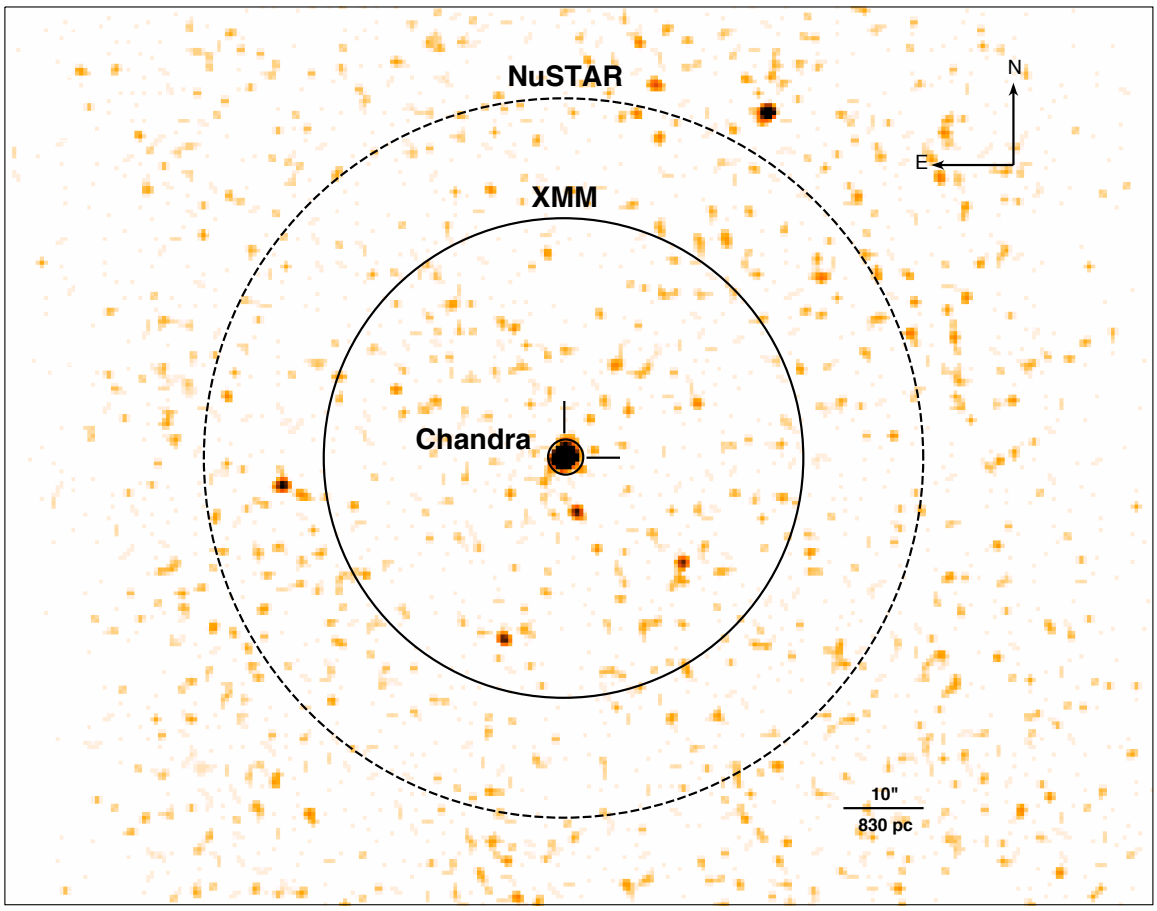

Fig. S1. Chandra image of the region around NGC 5907 ULX. *Chandra* ACIS-S 0.2–10 keV (observation identification number: 12987) image of the $120'' \times 120''$ region around NGC 5907 ULX with superimposed the *XMM–Newton* (solid line) and *NuSTAR* (stepped line) regions used in this work to extract the source events. In order to emphasize the sources the *Chandra* imaged has been smoothed by using a $2''$-radius Gaussian function. At the distance of 17.1 Mpc, an angular separation of $10''$ correspond to about 830 pc.

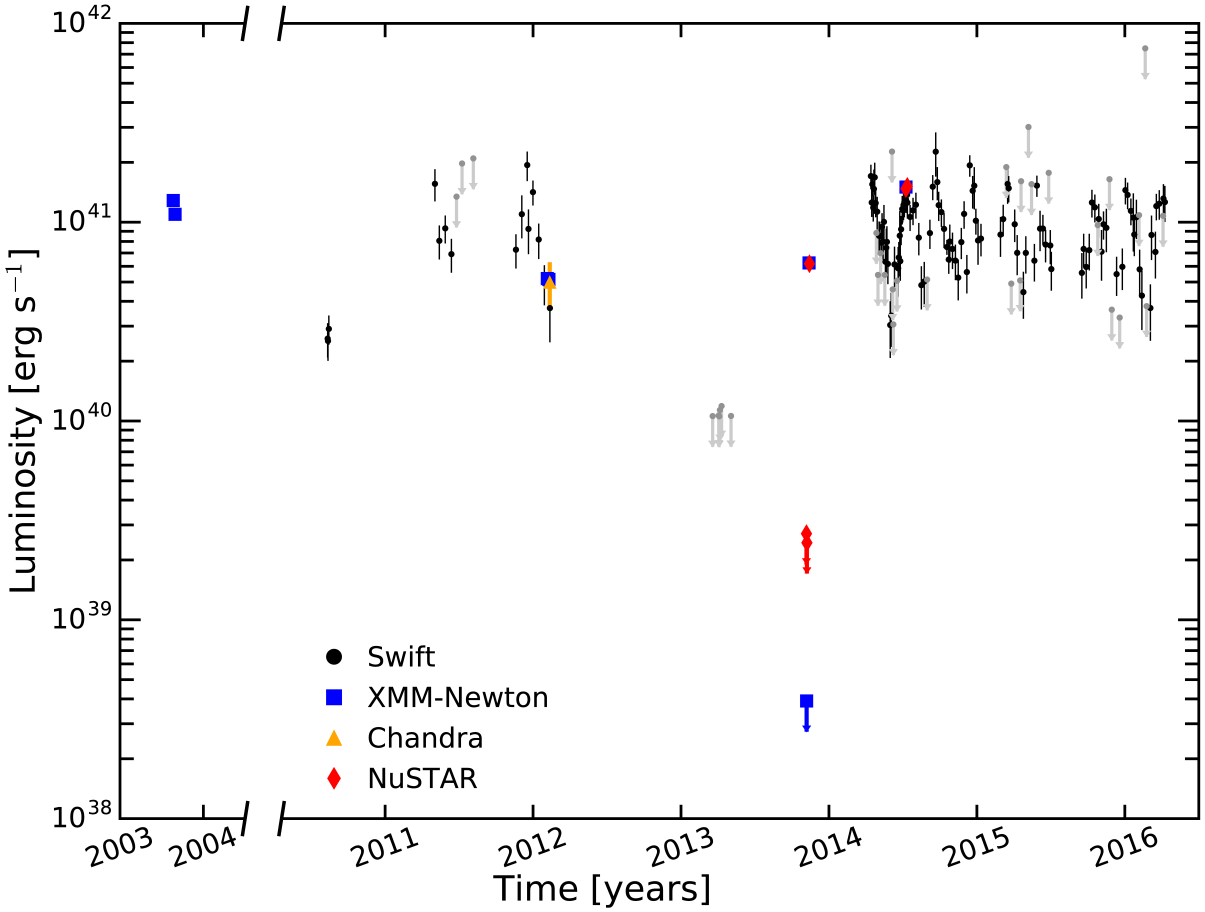

Fig. S2. Long-term light curve of NGC 5907 ULX. Long-term multi-mission light curve of NGC 5907 ULX. The luminosity was computed assuming a distance of 17.1 Mpc. All errors are at 1σ confidence level, while upper limits (red, blue and grey down arrows for *NuSTAR*, *XMM–Newton* and *Swift*, respectively) are at 3σ level.

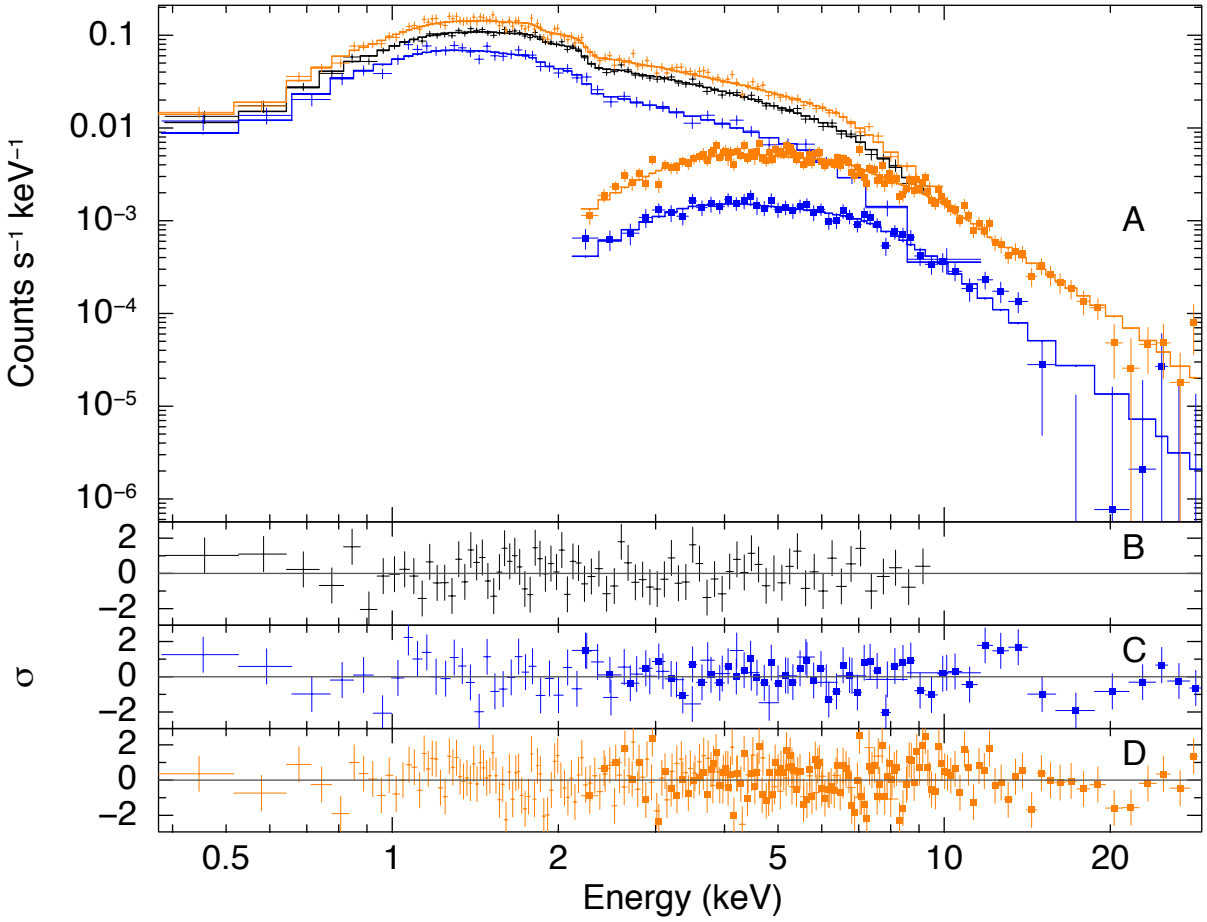

Fig. S3. Spectral energy distribution of NGC 5907 ULX. *XMM–Newton* EPIC pn (crosses) and *NuSTAR* FPM (squares) spectra collected in 2003 (black, only pn), 2013 (blue), and 2014 (orange; panel A). For the two latest epochs, the *XMM–Newton* and *NuSTAR* data are simultaneous. The solid lines show the broken power-law model. Lower panel: The residuals (in units of standard deviation) are reported separately for the three epochs: 2003 (panel B), 2013 (panel C) and 2014 (panel D).

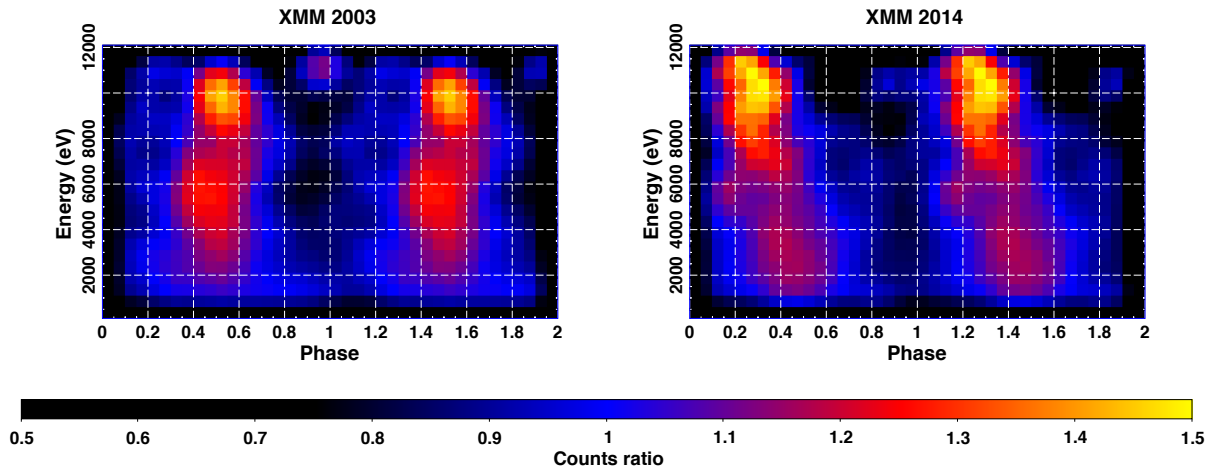

Fig. S4. Energy–phase distribution of NGC 5907 ULX. Phase-energy images obtained by binning the EPIC pn source counts into 20 phase bins and energy channels of 500 eV for the 2003 (left panel) and 2014 (right panel) *XMM–Newton* observations. The color scale represents the ratio between the counts in each phase interval and the phase-averaged counts in the same energy bin. A pulse peak shift is evident in the 2014 dataset.

Table S1. X-ray observations log. The bolometric luminosity is inferred by assuming a distance of 17.1 Mpc and extrapolating the result of the fit with a broken power-law model. Uncertainties are at 1σ confidence level. Upper limits are at 3σ level. The symbol (*) marks the observations during which pulsations were detected. The full table is available in a separate text file as part of the supplementary material.

Observation id.	Mission/Instr.	Start date (yyyy-mm-dd)	Net exposure (s)	Luminosity (10^{40} erg s^{-1})
0145190201*	*XMM–Newton*/EPIC	2003-02-20	36898	12.9 ± 0.1
0145190101	*XMM–Newton*/EPIC	2003-02-28	42095	11.0 ± 0.1
00031785001	*Swift*/XRT	2010-08-12	5516	2.6 ± 0.3
00031785002	*Swift*/XRT	2010-08-13	5151	2.5 ± 0.3
00031785003	*Swift*/XRT	2010-08-15	6710	2.9 ± 0.3
00031785005	*Swift*/XRT	2011-05-04	1178	15.7 ± 1.9
00031785006	*Swift*/XRT	2011-05-15	1905	8 ± 1
00031785007	*Swift*/XRT	2011-05-29	2552	9 ± 1
00031785008	*Swift*/XRT	2011-06-13	2102	7.0 ± 0.9
00031785009	*Swift*/XRT	2011-06-26	254	<13
00031785010	*Swift*/XRT	2011-07-10	172	<20
00031785011	*Swift*/XRT	2011-08-07	162	<22
00031785012	*Swift*/XRT	2011-11-20	2040	7.3 ± 0.9
00031785013	*Swift*/XRT	2011-12-04	899	11 ± 2
00031785014	*Swift*/XRT	2011-12-18	951	20 ± 2
00031785015	*Swift*/XRT	2011-12-21	916	9 ± 1
00031785016	*Swift*/XRT	2012-01-01	1860	14 ± 1
00031785017	*Swift*/XRT	2012-01-15	1655	8 ± 1
00031785018	*Swift*/XRT	2012-01-29	2157	5.0 ± 0.7
0673920201	*XMM–Newton*/EPIC	2012-02-05	14993	5.3 ± 0.1
0673920301	*XMM–Newton*/EPIC	2012-02-09	15024	5.1 ± 0.1
12987	*Chandra*/ACIS-S	2012-02-11	15977	5.0 ± 0.8
14391	*Chandra*/ACIS-S	2012-02-11	13086	5.0 ± 0.8
00031785019	*Swift*/XRT	2012-02-12	1445	3.7 ± 0.8
00032764001	*Swift*/XRT	2013-03-19	3958	<1
00032764002	*Swift*/XRT	2013-04-03	3925	<1
00032764003	*Swift*/XRT	2013-04-04	3970	<2
00032764004	*Swift*/XRT	2013-04-06	3643	<1
00032764005	*Swift*/XRT	2013-04-10	3451	<1
00032764006	*Swift*/XRT	2013-05-04	3950	<1
0724810201	*XMM–Newton*/EPIC	2013-11-06	30341	<0.04
30002039002	*NuSTAR*/FPM	2013-11-06	45339	<0.3
30002039003	*NuSTAR*/FPM	2013-11-06	68542	<0.3
0724810401	*XMM–Newton*/EPIC	2013-11-12	29961	6.2 ± 0.1
30002039005	*NuSTAR*/FPM	2013-11-12	112924	6.2 ± 0.1
00032764007	*Swift*/XRT	2014-04-14	1828	17 ± 2
00032764008	*Swift*/XRT	2014-04-16	1927	12 ± 1
00032764009	*Swift*/XRT	2014-04-18	2245	16 ± 1
00032764010	*Swift*/XRT	2014-04-20	2160	12 ± 1
00032764011	*Swift*/XRT	2014-04-22	914	14 ± 2
00032764012	*Swift*/XRT	2014-04-24	938	17 ± 2
00032764013	*Swift*/XRT	2014-04-26	1935	12 ± 1
00032764014	*Swift*/XRT	2014-04-28	392	23 ± 3

Table S1 — Continued

Observation id.	**Mission/Instr. (yyyy-mm-dd)**	**Start/Stop time (s)**	**Net exposure (10^{40} erg s^{-1})**	**Luminosity**[a]
00032764015	*Swift*/XRT	2014-04-30	1583	11±1
00032764016	*Swift*/XRT	2014-05-02	649	<6
00032764017	*Swift*/XRT	2014-05-04	1972	9±1
00032764018	*Swift*/XRT	2014-05-06	2042	9±1
00032764019	*Swift*/XRT	2014-05-08	499	<8
00032764020	*Swift*/XRT	2014-05-10	1900	8±1
00032764021	*Swift*/XRT	2014-05-12	1927	12±1
00032764022	*Swift*/XRT	2014-05-14	1937	8±1
00032764023	*Swift*/XRT	2014-05-16	1485	9±1
00032764024	*Swift*/XRT	2014-05-18	649	<6
00032764025	*Swift*/XRT	2014-05-20	1688	6±1
00032764026	*Swift*/XRT	2014-05-22	2067	8±1
00032764027	*Swift*/XRT	2014-05-24	1897	8±1
00032764028	*Swift*/XRT	2014-05-26	2075	8±1
00032764029	*Swift*/XRT	2014-06-01	2015	3.1±0.6
00032764030	*Swift*/XRT	2014-06-03	1853	3.4±0.7
00032764031	*Swift*/XRT	2014-06-05	149	<23
00032764032	*Swift*/XRT	2014-06-07	774	<5
00032764033	*Swift*/XRT	2014-06-09	1193	<3
00032764034	*Swift*/XRT	2014-06-11	1673	6±1
00032764035	*Swift*/XRT	2014-06-18	696	<5
00032764036	*Swift*/XRT	2014-06-20	1952	6±1
00032764037	*Swift*/XRT	2014-06-22	2082	6±1
00032764038	*Swift*/XRT	2014-06-24	586	9±2
00032764039	*Swift*/XRT	2014-06-26	2065	6.4±0.8
00032764040	*Swift*/XRT	2014-06-28	2097	9±1
00032764041	*Swift*/XRT	2014-06-30	1790	12±1
00032764042	*Swift*/XRT	2014-07-02	2609	11±1
00032764043	*Swift*/XRT	2014-07-04	1840	12±1
00032764044	*Swift*/XRT	2014-07-06	1887	12±1
0729561301[b]	*XMM–Newton*/EPIC	2014-07-09	37569	15.0±0.1
80001042002[b]	*NuSTAR*/FPM	2014-07-09	57113	14.7±0.2
00080756001	*Swift*/XRT	2014-07-10	1937	8±1
00080756002	*Swift*/XRT	2014-07-12	1872	14±1
80001042004[b]	*NuSTAR*/FPM	2014-07-12	56312	15.2±0.2
00032764045	*Swift*/XRT	2014-07-13	1600	12±1
00032764046	*Swift*/XRT	2014-07-20	2290	11±1
00032764047	*Swift*/XRT	2014-07-27	1947	11±1
00032764048	*Swift*/XRT	2014-08-03	1945	12±1
00032764049	*Swift*/XRT	2014-08-10	1955	12±1
00032764050	*Swift*/XRT	2014-08-17	1912	4.8±0.8
00032764051	*Swift*/XRT	2014-08-24	1658	5.1±0.8
00032764052	*Swift*/XRT	2014-08-31	686	<5
00032764053	*Swift*/XRT	2014-09-07	2205	11±1

Table S1 — Continued

Observation id.	**Mission/Instr. (yyyy-mm-dd)**	**Start/Stop time (s)**	**Net exposure (10^{40} erg s^{-1})**	**Luminosity**[a]
00032764054	*Swift*/XRT	2014-09-14	1723	14±1
00032764055	*Swift*/XRT	2014-09-21	392	23±3
00032764056	*Swift*/XRT	2014-09-25	1031	16±2
00032764057	*Swift*/XRT	2014-09-28	1585	12±1
00032764058	*Swift*/XRT	2014-10-05	1975	11±1
00032764059	*Swift*/XRT	2014-10-12	1902	9±1
00032764060	*Swift*/XRT	2014-10-19	9589	7.4±0.4
00032764061	*Swift*/XRT	2014-10-23	3835	6.5±0.6
00032764062	*Swift*/XRT	2014-10-26	1445	3.7±0.8
00032764063	*Swift*/XRT	2014-11-02	1748	8±1
00032764064	*Swift*/XRT	2014-11-09	2195	6.4±0.8
00032764065	*Swift*/XRT	2014-11-16	2270	5.3±0.8
00032764066	*Swift*/XRT	2014-11-23	2232	8±1
00032764067	*Swift*/XRT	2014-11-30	1920	11±1
00032764068	*Swift*/XRT	2014-12-07	2000	5.6±0.8
00032764069	*Swift*/XRT	2014-12-14	2012	19±2
00032764070	*Swift*/XRT	2014-12-21	1046	14±2
00032764071	*Swift*/XRT	2014-12-25	953	15±2
00032764072	*Swift*/XRT	2014-12-29	2427	11±1
00032764073	*Swift*/XRT	2015-01-04	1383	8±1
00032764074	*Swift*/XRT	2015-01-11	1970	8±1
00032764075	*Swift*/XRT	2015-02-28	1430	9±1
00032764076	*Swift*/XRT	2015-03-07	1680	11±1
00032764077	*Swift*/XRT	2015-03-14	179	<19
00032764078	*Swift*/XRT	2015-03-18	816	10±3
00032764079	*Swift*/XRT	2015-03-20	1910	16±1
00032764080	*Swift*/XRT	2015-03-27	721	<5
00032764081	*Swift*/XRT	2015-04-04	1573	9±1
00032764082	*Swift*/XRT	2015-04-10	1555	8±1
00032764083	*Swift*/XRT	2015-04-18	694	<5
00032764084	*Swift*/XRT	2015-04-20	212	<16
00032764085	*Swift*/XRT	2015-04-26	1932	4.5±0.8
00032764086	*Swift*/XRT	2015-05-02	1805	8±1
00032764087	*Swift*/XRT	2015-05-08	112	<29
00032764088	*Swift*/XRT	2015-05-16	219	<16
00032764089	*Swift*/XRT	2015-05-23	2262	4±1
00032764090	*Swift*/XRT	2015-05-29	2459	16±1
00032764091	*Swift*/XRT	2015-06-06	1206	9±1
00032764092	*Swift*/XRT	2015-06-13	1975	11±1
00032764093	*Swift*/XRT	2015-06-19	2325	8±1
00032764094	*Swift*/XRT	2015-06-27	192	<17
00032764095	*Swift*/XRT	2015-07-01	1853	3.4±0.7
00032764096	*Swift*/XRT	2015-07-04	1915	5.9±0.8
00032764097	*Swift*/XRT	2015-09-17	1480	5.6±0.9

Table S1 — Continued

Observation id.	**Mission/Instr. (yyyy-mm-dd)**	**Start/Stop time (s)**	**Net exposure (10^{40} erg s^{-1})**	**Luminosity**[a]
00032764098	*Swift*/XRT	2015-09-21	2057	8 ± 1
00032764099	*Swift*/XRT	2015-09-28	1905	8 ± 1
00032764100	*Swift*/XRT	2015-10-05	2030	8 ± 1
00032764101	*Swift*/XRT	2015-10-12	1733	12 ± 1
00032764102	*Swift*/XRT	2015-10-19	1810	12 ± 1
00032764103	*Swift*/XRT	2015-10-26	357	<9
00032764104	*Swift*/XRT	2015-10-29	1448	11 ± 1
00032764105	*Swift*/XRT	2015-11-04	926	8 ± 1
00032764106	*Swift*/XRT	2015-11-09	2135	9 ± 1
00032764107	*Swift*/XRT	2015-11-16	931	9 ± 1
00032764109	*Swift*/XRT	2015-11-24	207	<17
00032764110	*Swift*/XRT	2015-11-30	993	<3
00032764111	*Swift*/XRT	2015-12-12	2002	5.5 ± 0.8
00032764112	*Swift*/XRT	2015-12-19	1096	<3
00032764113	*Swift*/XRT	2015-12-26	1808	6 ± 1
00032764114	*Swift*/XRT	2016-01-02	1613	14 ± 1
00032764115	*Swift*/XRT	2016-01-08	1620	14 ± 1
00032764116	*Swift*/XRT	2016-01-16	1967	11 ± 1
00032764117	*Swift*/XRT	2016-01-22	496	11 ± 2
00032764118	*Swift*/XRT	2016-01-24	1480	5.6 ± 0.9
00032764119	*Swift*/XRT	2016-01-30	1668	11 ± 2
00032764120	*Swift*/XRT	2016-02-05	317	<11
00032764121	*Swift*/XRT	2016-02-07	1410	6 ± 1
00032764122	*Swift*/XRT	2016-02-12	1216	4.3 ± 0.9
00032764123	*Swift*/XRT	2016-02-20	44	<74
00032764124	*Swift*/XRT	2016-02-24	951	20 ± 2
00032764126	*Swift*/XRT	2016-03-04	1648	3.7 ± 0.8
00032764127	*Swift*/XRT	2016-03-07	1675	9 ± 1
00032764129	*Swift*/XRT	2016-03-17	1246	8 ± 1
00032764130	*Swift*/XRT	2016-03-19	1947	12 ± 1
00032764131	*Swift*/XRT	2016-03-26	1550	12 ± 1
00032764132	*Swift*/XRT	2016-04-04	319	<11
00032764133	*Swift*/XRT	2016-04-05	1278	12 ± 2
00032764134	*Swift*/XRT	2016-04-09	1111	12 ± 2

[a] The isotropic bolometric luminosity is inferred by assuming a distance of 17.1 Mpc. Uncertainties are at 1σ level and upper limits at 3σ level in the same band.
[b] Observations during which pulsations were detected.